MDPI

Highly Efficient Removal of Cu(II) Ions from Acidic Aqueous Solution Using ZnO Nanoparticles as Nano-adsorbents

Eduardo Leiva [1,2,*], Camila Tapia [1,3] and Carolina Rodríguez [1]

[1] Departamento de Química Inorgánica, Facultad de Química y de Farmacia, Pontificia Universidad Católica de Chile, Avenida Vicuña Mackenna 4860, Macul, Santiago 7820436, Chile; camilatapiape@gmail.com (C.T.); cnrodriguez@uc.cl (C.R.)
[2] Departamento de Ingeniería Hidráulica y Ambiental, Pontificia Universidad Católica de Chile, Avenida Vicuña Mackenna 4860, Macul, Santiago 7820436, Chile
[3] Departamento de Química, Facultad de Ciencias, Universidad de Chile, Ñuñoa 7800003, Chile
* Correspondence: ealeiva@uc.cl; Tel.: +56-2-2354-7224; Fax: +56-2-2354-5876

Abstract: Water pollution by heavy metals has significant effects on aquatic ecosystems. Copper is one of the heavy metals that can cause environmental pollution and toxic effects in natural waters. This encourages the development of better technological alternatives for the removal of this pollutant. This work explores the application of ZnO nanoparticles (ZnO-NPs) for the removal of Cu(II) ions from acidic waters. ZnO NPs were characterized and adsorption experiments were performed under different acidic pHs to evaluate the removal of Cu(II) ions with ZnO NPs. The ZnO NPs were chemically stable under acidic conditions. The adsorption capacity of ZnO NPs for Cu(II) was up to 47.5 and 40.2 mg·g^{-1} at pH 4.8 and pH 4.0, respectively. The results revealed that qmax (47.5 mg·g^{-1}) and maximum removal efficiency of Cu(II) (98.4%) are achieved at pH = 4.8. In addition, the surface roughness of ZnO NPs decreases approximately 70% after adsorption of Cu(II) at pH 4. The Cu(II) adsorption behavior was more adequately explained by Temkin isotherm model. Additionally, adsorption kinetics were efficiently explained with the pseudo-second-order kinetic model. These results show that ZnO NPs can be an efficient alternative for the removal of Cu(II) from acidic waters and the adsorption process was more efficient under pH = 4.8. This study provides new information about the potential application of ZnO NPs as an effective adsorbent for the remediation and treatment of acidic waters contaminated with Cu(II).

Keywords: adsorption; copper; zinc-oxide nanoparticles; nanomaterials; acid mine drainage

1. Introduction

Surface and groundwater contamination by heavy metals is a growing concern. One of the major sources of heavy metals is the contamination derived from acid mine drainage (AMD) release [1–3]. AMD is characterized by low pH and high concentrations of sulfate and dissolved metals and metalloids, causing severe damage to aquatic ecosystems [1,2]. Among the metals that are commonly released are iron, copper, lead, zinc, silver, arsenic, aluminum, manganese, antimony, selenium, among others [4]. Heavy metals and metalloids affect the quality of surface and groundwater resources, mainly because they are non-biodegradable, toxic at low concentrations, and easy to accumulate in the tissues of various living organisms [5,6]. They can cause serious harm to human health from cancer to nervous system problems [7–9]. Thus, the study and development of sustainable technologies to remove these pollutants have gained attention in recent years.

One of the metals that are most widely present in surface waters is copper, mainly because of its multiple industrial applications [10–12]. In addition, many mining operations release acid runoff with high Cu concentrations, affecting unique ecosystems [13,14]. In native systems, Cu is usually found as a divalent cation (Cu(II)) and is quite mobile at

low pH values, which makes the treatment of copper-enriched AMD more and more relevant [15]. Copper is quite toxic even at low concentrations and its antimicrobial effects can cause substantial damage to the biodiversity of both microorganisms and higher organisms [16]. Thus, polluted waters with copper must be treated to reduce their impact on the environment [16]. The World Health Organization (WHO) establishes that the maximum limit of the concentrations of copper ions in drinking water should not exceed 2 mg·L^{-1}. In recent years, significant efforts have been made to develop technologies for the treatment and removal of copper from polluted waters, in order to respond to the environmental effects of copper and the projected scarcity of water resources. In this context, technologies based on adsorption, ion exchange, photocatalysis, filtration and reverse osmosis methods have been extensively studied [16–27]. However, adsorption methods are the most cost-effective and have been the subject of various studies. The costs associated with adsorption technologies for water treatment vary from USD 10 to 200 per million liters [28,29] while the other conventional technologies such as ion exchange, reverse osmosis, ultrafiltration and electrodialysis have costs ranging from USD 15 to 450 per million liters [29] (Appendix A). Despite this, in recent years improvements in the removal process based on the use of nano-adsorbents have emerged as an alternative that can improve the adsorption capacity because of characteristic properties of nanomaterials such as higher surface area and greater potential for functionalization.

Various materials have been studied for the removal of Cu from wastewaters. The use of adsorbent materials based on carbon, such as activated carbon and graphene, has shown to be a suitable alternative for the removal of Cu, with adsorption capacities over 30 and 40 mg/g, respectively [30,31]. Other adsorbents studied at low pH have presented variable efficiency, with adsorption capacities of 20.97 and 31.7 mg/g for waste slurry and pecan shells activated carbon, respectively [32,33]. In addition, some nanomaterials that have shown high efficiency to remove copper from polluted waters are graphene oxides [34], biopolymers-based adsorbents [35,36], organic polymers [37], magnetic nanoparticles [38,39] carbon nanotubes [40–42], silica-based nanomaterials [43], metallic NPs [44]. Among the metallic nanoparticles that have been studied for the removal and adsorption of heavy metals, Zinc oxide (ZnO) has shown excellent results because of its catalytic properties. ZnO nanoparticles (NPs) have a high potential to be used as nano-adsorbents since they have a large specific surface area and various functional groups that favor their interaction and removal of heavy metals from aqueous solutions [45]. It has other advantages, such as high resistance to chemical and optical corrosion, high chemical stabilization, biocompatibility, environmentally friendly and is non-toxic in nature [46,47]. On one hand, ZnO NPs have antibacterial properties that inhibit the growth of both Gram-positive and Gram-negative bacteria, which may be optimal as an antifouling mechanism in sorbent media [48,49]. ZnO NPs are cheap compared to carbon-based nanomaterials, can be produced on a large scale, have a good photocatalytic performance and have a high removal efficiency of various inorganic pollutants such as heavy metals [47,48,50]. Li et al., 2014 [51] reported that ZnO NPs can adsorb heavy metals by the various kinds of hydroxyl groups present on their surface. Several studies have used ZnO for the removal of toxic pollutants, such as Cr (VI), Ni(II), Pb(II) [52–56]. However, few studies have focused on the removal of Cu(II) [57,58]. Wang et al. [59] showed that ZnO particles encapsulated in hollow microspheres are more efficient for the removal of Cu(II), Cd(II) and Pb(II) cations than commercial ZnO particles. Meanwhile, Primo et al., 2020 [60] showed a high removal of Cu(II) ions with ZnO NPs synthesized using the Aloe vera green synthesis route. Despite this, there are very few studies that have focused on the removal of Cu(II) from acidic waters where Cu(II) ions can be found in higher concentrations. Indeed, the adsorption of Cu(II) ions onto ZnO NPs is poorly covered in the literature, and there are practically no studies in acidic waters. Hence, the relevance of pH in the adsorption efficiency of Cu(II) should be studied to evaluate the potential scaling of ZnO nano-adsorbents in acidic water treatment technologies.

In this work, we presented our preliminary results about the use ZnO NPs as nanoadsorbents of Cu(II) ions from AMD waters. Cu(II) removal rates were evaluated in batch adsorption tests under different pHs. Experimental data were fitted using different isotherms models in adsorption experiments. Using ZnO NPs has the advantage of having a good cost-effectiveness ratio compared to other nanomaterials such as graphene, CNTs and magnetic nanoparticles (Appendix B). The study of the adsorption capacity under different pHs will allow exploring potential uses as emerging and sustainable technologies for the removal of Cu(II) from AMD waters. In addition, knowing the removal effectiveness in AMD waters allows determining its chemical and functional stability under more aggressive conditions, which can give it a comparative advantage compared with other commercial adsorbents and can promote effective scaling in real conditions.

2. Materials and Methods

2.1. Materials

Commercially produced ZnO NPs (≤100 nm) were purchased from SigmaAldrich (St. Louis, MO, USA) and in this study were used without further purification. Cooper-enriched synthetic acid wastewater was prepared by adding $NaNO_3$ and $CuSO_4 \cdot 5H_2O$ to deionized (DI) water. Sulfuric acid (H_2SO_4), hydrochloric acid (HCl), and absolute ethanol (C_2H_5OH) were purchased from Merck. All the reagents and solvents used were of analytical reagent grade and all solutions were prepared with deionized (DI) water.

2.2. Preparation of ZnO Nanoadsorbents

ZnO NPs with an average size of 100 nm were used in batch adsorption experiments. The ZnO NPs suspension was obtained through the dispersion into absolute ethanol (0.33 mg·mL^{-1}), and then the solution was sonicated for 40 min. Finally, the ZnO NPs were separated from the liquid by centrifugation (4000 rpm, t = 30 min), washed three times with ethanol and kept hermetically sealed until their use in adsorption studies.

2.3. Characterization Techniques

Prior to adsorption experiments, ZnO NPs were characterized using Raman spectroscopy, scanning electron microscope (SEM) coupled with energy-dispersive X-ray spectroscopy (SEM-EDX), field emission scanning electron microscopy (FESEM) and Brunauer–Emmett–Teller analysis.

Raman spectra were recorded using WITec Alpha 300 RA confocal Raman microscope with AFM (WITec GmbH, Ulm, Germany). The scanning electron micrographs were determined by using a scanning electron microscope (SEM) (JSM-IT300LV, JEOL, Tokyo, Japan) coupled with energy-dispersive X-ray spectroscopy (Oxford Instruments, High Wycombe, UK) (SEM-EDX). The scanning electron micrographs (SEM-EDX) were used to confirm the nanoparticle size and elemental mapping on the nanometer scale of ZnO NPs. On the other hand, field emission scanning electron microscopy (FESEM) images of the ZnO NPs were obtained using a scanning electron microscope (Quanta 250 FEG, FEI Co., Hillsboro, OR, USA) equipped with an EDX (XFlash 5010; Bruker AXS Microanalysis, Berlin, Germany). The FESEM images were used to analyze the surface topography and fine morphology of the ZnO NPs.

The specific surface area and pore volume of the ZnO NPs were determined by Brunauer–Emmett–Teller analysis (BET) N2 adsorption–desorption analysis (Micromeritics Instruments Corp., Norcross, GA, USA). Finally, the pH of the point of zero charge (pH$_{PZC}$) and zeta potential for ZnO NPs was determined by adjusting 0.01 M NaCl solutions to different pH values from 2 to 12 using 0.1 M NaOH and 0.1 M HCl added dropwise. Then, 30 mg of ZnO NPs were added to test tubes with 40 mL of the different pH solutions and shaken at 380 rpm at room temperature for 24 h. The final pH and zeta potential were measured using a pH meter (PHC301, HACH, Loveland, CO, USA) [41,61].

2.4. Batch Adsorption Studies

Equilibrium isotherms for Cu(II) were obtained in batch adsorption studies using ZnO NPs as nano-adsorbents. Experiments were performed Cu(II) concentrations ranging between 3.0 and 24.0 mg·L^{-1}. The Cu(II) solution was prepared by adding CuSO$_4$·5H$_2$O to deionized (DI) water.

The experiments were performed under two pHs: (1) with the resulting pH of the prepared solutions (Cu(II) solution + ZnO NPs) (pH = 4.8), and (2) with the pH adjusted to 4 by adding 0.01 M HCl (pH = 4.0) drop-wise and with continuous pH measurement until pH 4.0 was reached. For batch experiments, 20 mg of the ZnO NPs were added into 40 mL tubes with variable concentrations of Cu(II). The experiments were conducted in triplicate with shaking (380 rpm) in the dark at room temperature for 20 h for adsorption/desorption equilibrium. After the solutions reached equilibrium, they were centrifuged (6000 rpm, 5 min) to separate the solution from the ZnO NPs. The resulting supernatant was then filtered using 0.22 μm membranes to analyze the residual Cu(II) concentrations. Scanning electron microscopy (SEM) coupled with energy-dispersive X-ray spectroscopy (SEM-EDX) was used to analyze the morphology and elemental composition of the surface of ZnO NPs before and after Cu(II) adsorption in batch experiments.

The sorption capacity at equilibrium C_e (mg·g^{-1} sorbent) was calculated using Equation (1):

$$q_e = \frac{(C_0 - C_e) \cdot V}{m},$$ (1)

where C_0, C_e, V, and m correspond to the initial concentration (mg·L^{-1}), the aqueous-phase equilibrium metal concentration (mg·L^{-1}), the volume of suspension (L), and the mass of the adsorbent (g), respectively.

Similarly, the Cu(II) ions removal efficiency (η) of ZnO particles was calculated using Equation (2):

$$\eta\,(\%) = \left(\frac{C_0 - C_t}{C_0}\right) \cdot 100,$$ (2)

where C_0 and C_t were the concentration of metal ions at the initial and time t, respectively.

To study the effect of other ions on adsorption efficiency, multimetallic water was prepared at three different concentrations: (1) 3 mg·L^{-1} of Cu (Added as CuSO$_4$·5H$_2$O), Mn (Added as MnSO$_4$·H$_2$O) and Al (Added as KAl(SO$_4$)$_2$·12H$_2$O); (2) 12 mg·L^{-1} of Cu, Mn and Al; and (3) 22 mg·L^{-1} of Cu, Mn an Al. In this way, it is sought to emulate more realistic wastewater, with the presence of other ions in the solution.

2.5. Adsorption Isotherms

From data obtained experimentally in batch configurations, the Langmuir, Freundlich and Temkin isotherm models were fitted. The Langmuir model assumed that the adsorption surface sites have identical energy and each adsorbate molecule (Cu(II) in this study) is positioned in a single place, forming a monolayer of sorption on the adsorbent surface [62,63]. On the contrary, the Freundlich model describes reversible heterogeneous adsorption without restricting the adsorption process to a single monolayer [64]. For this reason, the Freundlich isotherm predicts that the adsorbate concentration on the adsorbent will increase without saturation according to how to increase the adsorbate concentration in the liquid solution [65].

The sorption capacity q (mg·g^{-1} sorbent) was obtained using Langmuir, Freundlich and Temkin models. Temkin Model was used to evaluate if the adsorption behavior can be better described for another model [66]. For this, Equations (3)–(5) were used for each model, respectively [63].

Langmuir model:

$$q = \frac{q_L K_l C_e}{1 + K_L C_e},$$ (3)

where q_L is the amount of adsorption corresponding to a monolayer coverage, K_L is the Langmuir constant associated with the energy of adsorption, and C_e is the metal concentration at the equilibrium in an aqueous solution (mg·L⁻¹).

Freundlich model:

$$q = K_F C_e^{\frac{1}{n}}, \tag{4}$$

where K_F is the constant related to adsorption capacity, n corresponds to the constant associated with adsorption intensity, and C_e is the metal concentration at the equilibrium in aqueous solution (mg·L⁻¹).

Temkin model:

$$q = BInA_t C_e, \tag{5}$$

where B is an abbreviation of RT(bt)⁻¹, where R, T and bt represent the gas constant (8.314 J·mol⁻¹·K⁻¹), absolute temperature (K) and Temkin isotherm constant, respectively, A_t corresponds to the Temkin isotherm equilibrium binding constant (L·g⁻¹) and C_e is the metal concentration at the equilibrium in aqueous solution (mg·L⁻¹).

2.6. Surface Roughness Analysis

The surface roughness of the ZnO NPs was analyzed before and after Cu(II) adsorption. Specifically, Gwyddion software was used to examine the surface characteristics of SEM images of ZnO NPs [67]. Several surface roughness representative parameters were selected according to Zhao et al., 2019 [68]. The parameters selected were mean roughness (R_a), the mean square roughness (R_q), the surface skewness (R_{sk}) and the kurtosis coefficient (R_{ku}).

Roughness average (R_a) is the average deviation of all points roughness profile from a mean line over the evaluation length and is used to represent the mean value of the surface roughness of the sample [68]. R_a is calculated using Equation (6):

$$R_a = \frac{1}{N}\sum_{j=1}^{N}|r_j|, \tag{6}$$

where the N are the number of scanning points on the sample.

Root mean square roughness (R_q) is defined as the average of the measured height deviations taken within the evaluation length and measured from the mean line [68]. R_q is used to determine the degree of change in the surface roughness of a sample and is calculated using Equation (7):

$$R_q = \sqrt{\frac{1}{N}\sum_{j=1}^{N}r_j^2}, \tag{7}$$

The surface skewness (R_{sk}) is a measure of the asymmetry of the amplitude distribution function of the sample and quantifies the symmetry of the variation in a profile about its mean line [68]. Specifically, R_{sk} represents the integrity of the surface roughness of a specific sample [68]. Thus, a value of R_{sk} equal to zero shows that the surface height distribution is normal. A negative R_{sk} value shows that the surface height distribution is biased to the left, which represents that there is more area where the sample surface height is above the mean value. On the contrary, a positive R_{sk} value shows that the distribution is biased to the right and therefore there is more area where the sample surface height is below the mean value [68]. R_{sk} is calculated using Equation (8):

$$R_{sk} = \frac{1}{NR_q^3}\sum_{j=1}^{N}r_j^3, \tag{8}$$

Kurtosis (R_{ku}) is related to the uniformity of the amplitude distribution function of the sample [68]. A value of R_{ku} equal to zero shows that the surface height distribution of the sample follows a normal distribution. A negative value shows that the waveform associated with the surface height distribution is flat, so the surface height of the sample is

distributed throughout the sample, while a positive value of R_{ku} shows the waveform has a peak, and the surface height of the sample is concentrated at the mean value of one or several peaks [68]. R_{ku} is calculated using Equation (9):

$$R_{ku} = \frac{1}{NR_q^4} \sum_{j=1}^{N} r_j^4, \tag{9}$$

2.7. Kinetic Experiments

The kinetic behavior of Cu(II) adsorption with ZnO NPs was studied using 20 mg of ZnO NPs in 40 mL of Cu(II) solution. Cu(II) concentration used was 25 mg·L^{-1}. The solutions were shaken at 380 rpm at room temperature (22–25 °C) and sampling was performed at 10 min, 30 min, 1 h, 2 h, 4 h, and 24 h. The Cu(II) removal was plotted in function of time. In order to analyze the uptake rates of Cu(II) ions, a kinetic analysis using pseudo-first-order and pseudo-second-order kinetic equations was performed.

The pseudo-first-order kinetic model was represented by Equation (10) according to Ding et al. [69].

$$\log(q_e - q_t) = \log q_e - \frac{k_1}{2.303} t, \tag{10}$$

where k_1 corresponds to first-order adsorption constant (min^{-1}), q_e is the adsorption capacity at equilibrium (mg·g^{-1}), q_t is the adsorption capacity at the time t (mg·g^{-1}).

The pseudo-second-order kinetic model was represented by Equation (11) according to Ho and McKay [70].

$$\frac{t}{q_t} = \frac{1}{k_2 q_e^2} + \frac{t}{q_e}, \tag{11}$$

where k_2 is the second-order adsorption constant (g·mg^{-1}·min^{-1}), q_e is the adsorption capacity at equilibrium (mg·g^{-1}), q_t is the adsorption capacity at the time t (mg·g^{-1}).

The linearized form of these kinetic models was plotted. From the trend line of the experimental data, the kinetic constants and parameters were determined using the slope and intercept values obtained in each case.

The approaching equilibrium factor (R_w) was calculated to characterize the kinetic curve behavior of the pseudo-second-order model using Equation (12) according to Wu et al. [71]

$$R_w = \frac{1}{1 + k_2 q_e t_{ref}}, \tag{12}$$

where k_2 is the second-order adsorption constant (g·mg^{-1}·min^{-1}), q_e is the adsorption capacity at equilibrium (mg·g^{-1}) and t_{ref} is the longest operation time (based on kinetic experiments).

Finally, the Gibbs free energy (ΔG^0) was determined as a thermodynamic parameter that indicates the degree of the spontaneity of an adsorption process where a higher negative value indicates a more energetically favorable adsorption process [72]. The ΔG^0 parameter was determined as follows [73,74].

$$\Delta G^0 = -RT \ln K \tag{13}$$

where R, T and K is the gas constant (8.314 J·mol^{-1}·K^{-1}), absolute temperature (K) and the equilibrium constant (L·g^{-1}).

2.8. Chemical Analyzes

Cu(II) cations concentrations were measured using a UV-vis spectrophotometer (DR3900, Hach, Loveland, CO, USA) and pH (PHC301, Hach, Loveland, CO, USA) was measured to adjust pH of experimental solutions before batch adsorption experiments of second pH (pH adjusted to 4.0) and immediately after sample collection using a multimeter (Hq40d Multi, Hach, Loveland, CO, USA).

2.9. Quality Assurance/Quality Control (QA/QC)

Quality assurance/quality control (QA/QC) procedures were performed for all the analyzes carried out in this study, to ensure the quality, reproducibility, and accuracy of the obtained results. All equipment was calibrated prior to its use in this study and periodically during its development according to the instrument guidelines. All the chemical reagents used in this study were analytical grade. Additionally, all materials used in the experiments and sampling were neatly cleaned and rinsed with Milli-Q water.

The accuracy and precision of the measurements of Cu(II) were checked and compared against blank samples and synthetic standard samples of known concentration. The batch adsorption isotherms were carried out in triplicate and the analytical measurements of pH and Cu(II) were verified by performing triplicate readings.

3. Results and Discussion

3.1. Adsorbent Characterization

3.1.1. Raman Spectroscopy

Raman spectrum of ZnO NPs is shown in Figure 1. The main peaks are identified in the figure. There was no detectable variation in the peaks frequency of different points analyzed in different areas of the sample. The main peaks at 95 cm^{-1} and 438 cm^{-1} are characteristic of ZnO and correspond to phonon frequencies E$_2$low and E$_2$high, respectively [75,76]. The peak at 330 is associated with the process E$_2$high − E$_2$low [77]. Therefore, the peaks obtained in the Raman analysis are consistent with the characteristic peaks of ZnO. In summary, the analysis of this spectrum indicates that the NPs used in this study effectively correspond to ZnO NPs.
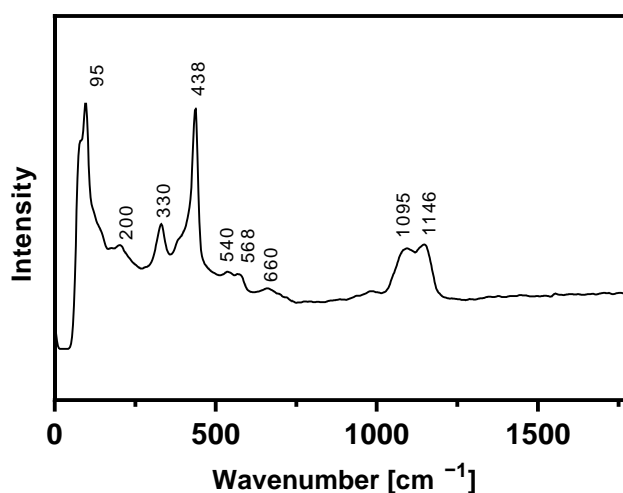

Figure 1. Raman spectrum of the ZnO NPs.

3.1.2. Brunauer–Emmett–Teller (BET) Analysis

Figure 2 shows adsorption/desorption curve of ZnO NPs. A hysteresis loop with typical characteristics of type H3 can be observed in isotherms, typical of type 3 and 5 isotherms. In addition, from the analysis, it can be observed that ZnO NPs showed higher values for BET surface area, reaching a value of 45.58 m^2·g^{-1}. The pore size distribution curve was determined using the Barrett–Joyner–Halenda (BJH) method. The average pore volume (Vp) and pore diameter (Dp) were found to be 30.87 nm and 0.3 cm^3·g^{-1}, respectively. Similar results were observed by Zafar et al. [78] reaching values 0.211 cm^3·g^{-1} for V$_P$ and 27.44 nm for D$_P$. These data show that ZnO NPs have a large exposed surface, which can favor surface adsorption processes of heavy metals.
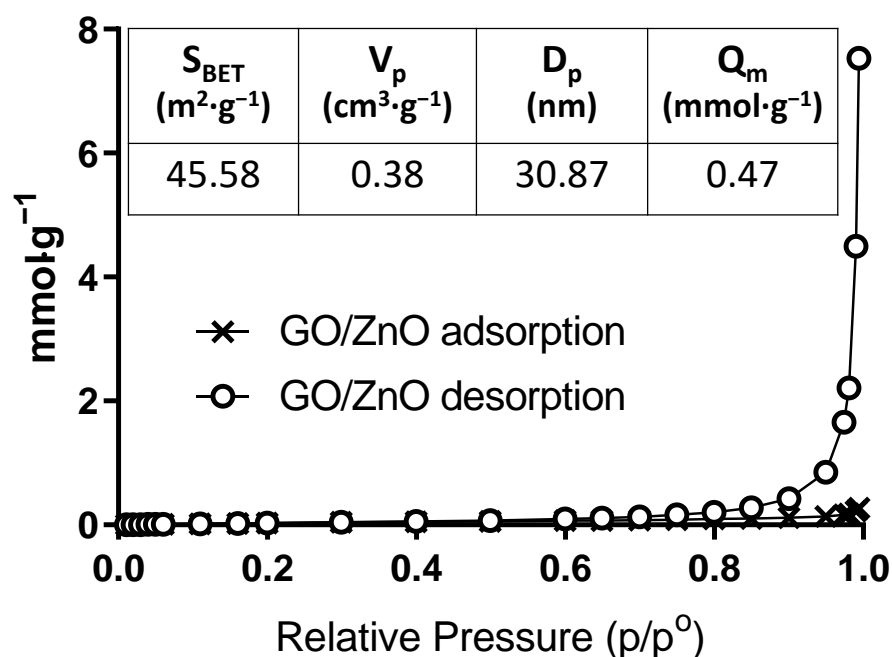
S_{BET} ($m^2{\cdot}g^{-1}$)	V_p ($cm^3{\cdot}g^{-1}$)	D_p (nm)	Q_m ($mmol{\cdot}g^{-1}$)
45.58	0.38	30.87	0.47

Figure 2. BET adsorption–desorption isotherms for ZnO NPs.

3.1.3. Scanning Electron Microscopy (SEM)

The morphology of ZnO NPs can be observed in Figure 3a,b. The ZnO NPs show small spherical particles with uniform shapes (Arrows). The different sizes of NPs could be a consequence of the formation of interconnected agglomerates between NPs, which could cause a decrease in the available surface area. The field emission scanning electron microscopy (FESEM) (images not shown) confirmed that the ZnO NPs are nano in size (<100 nm).

The surface chemical composition of ZnO NPs was determined by EDX analysis. The energy peaks of Zn and O are clear in EDX spectrum of ZnO NPs (Figure 3c). From the elemental analysis, it is observed that ZnO NPs, as expected, are composed of Zinc (59.6% wt) and Oxygen (40.4% wt). Furthermore, the absence of other peaks suggests that the purity of the NPs used in this study was high.
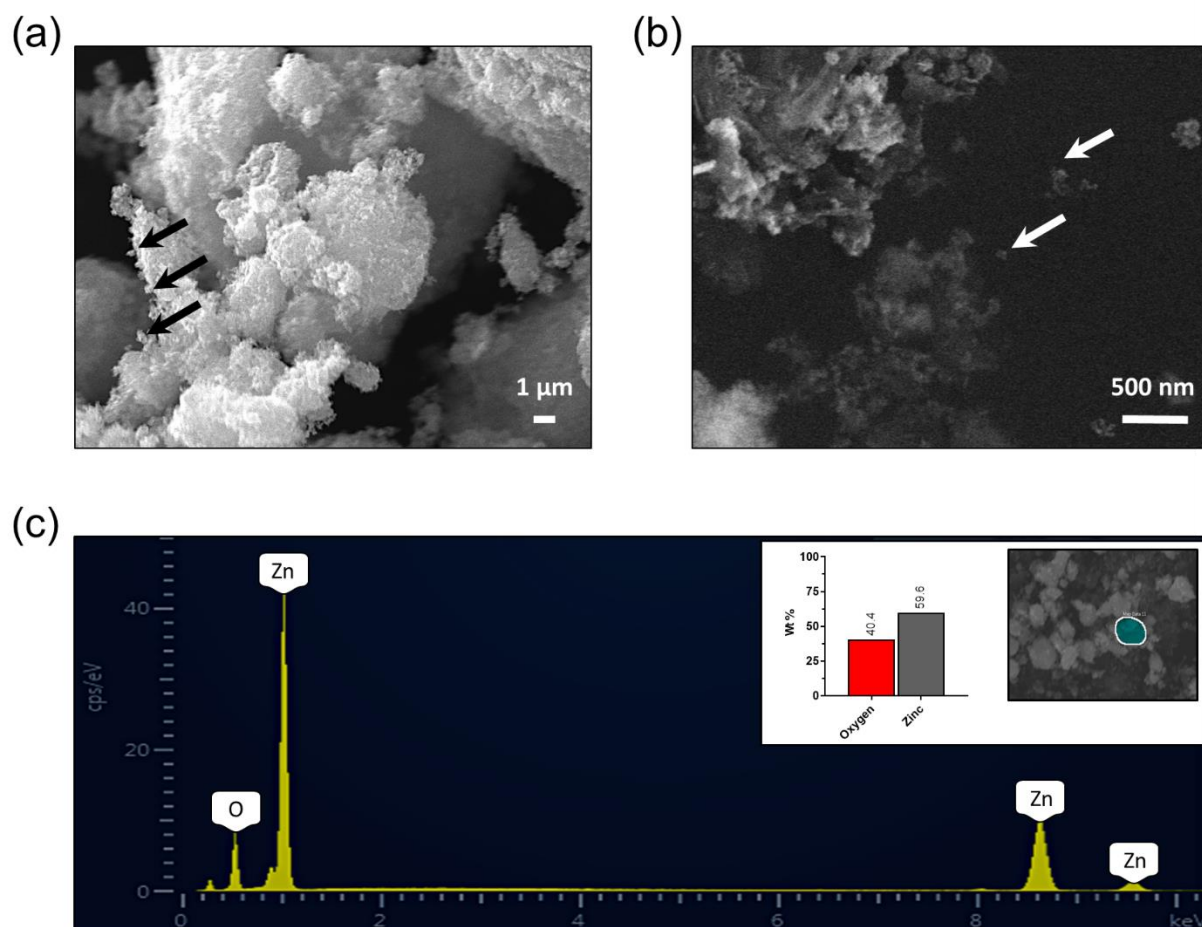
Figure 3. Scanning electron micrographs (**a**) and scanning transmission electron microscopy (STEM) (**b**) of ZnO NPs. Representative EDX spectrum and elemental mapping of ZnO NPs (**c**).

The pHpzc value was obtained for ZnO NPs through the plot of initial pH values and final pH (Figure 4a). A value of 6.21 for ZnO NPs was determined. Other studies have reported higher pHpzc values. For example, Kataria and Garg [79] reported pHpzc values of 6.9. Meanwhile, Chauhan et al. [80] reported pHpzc values of 7.5. The differences observed with other studies may be a consequence of the method of synthesis, the aggregation of the NPs, the presence of impurities, among other factors. The pHpzc corresponds to the pH in which the positive and negative charges are equal on the surface of an adsorbent [81]. Therefore, the surface of ZnO NPs will be positively charged if pH < pHpzc, while it will have a net negative charge if pH > pHpzc. This parameter is important for the heavy metal adsorption process by ZnO NPs, since at values higher than pH = 6.21 the ZnO NPs surface will be negatively charged enhanced electrostatic attraction between heavy metal cations (such as Cu(II)) and ZnO surface. On the contrary, at lower pH values (<pHpzc) the adsorption process will not be as effective as there are higher repulsive forces. Even so, the adsorption process is not determined solely by this parameter, but will also depend on the surface area, the density of pores, the presence of competitors, among other factors. Conversely, the measurement of the zeta potential reveals that the pH where the surface potential of the material is zero, the isoelectric point (IEP) [82] (Figure 4b), is 10.2, a value higher than that obtained at the pHPZC. The values of pHPZC and IEP must be

equal if H^+ and OH^- are the only potential determining ions. Therefore, the difference obtained between these two values may be because other specific adsorptions are occurring [83,84].
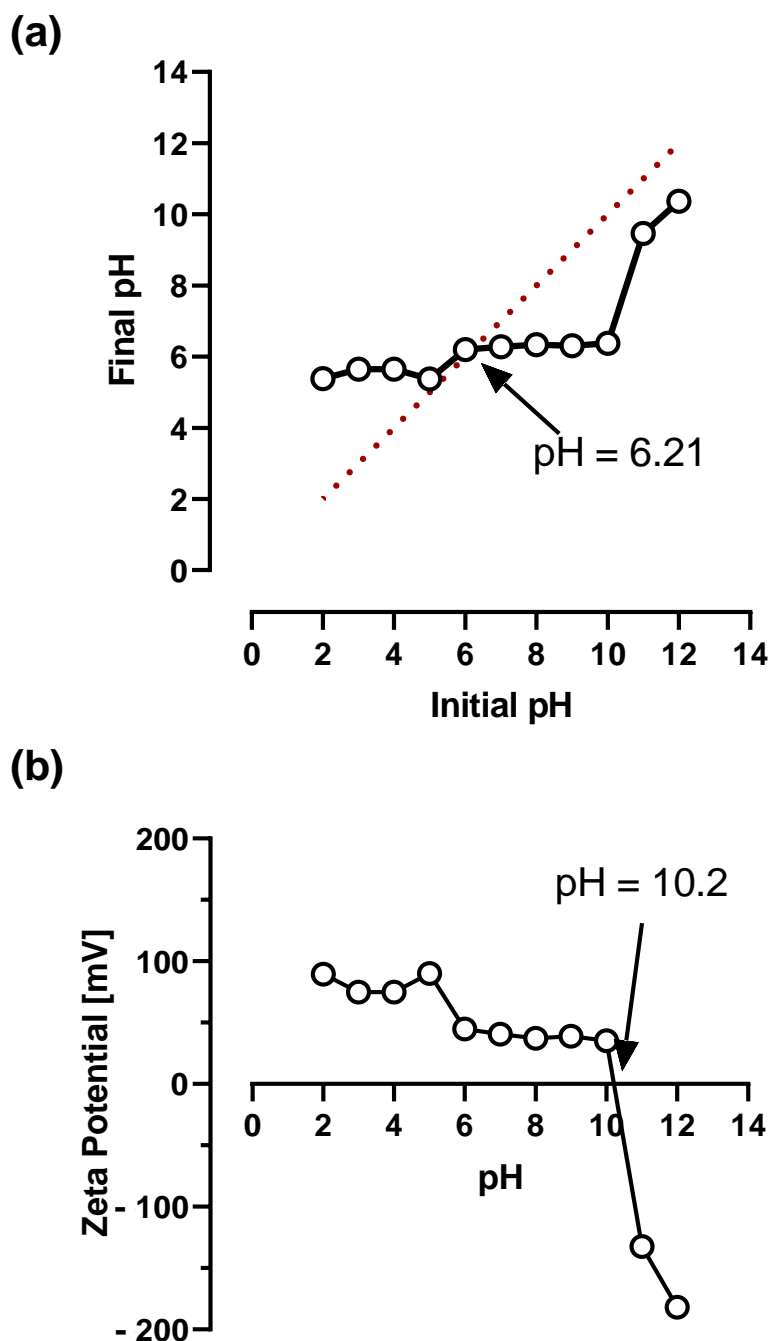
(a)

(b)

Figure 4. (**a**) Point zero charge (pHpzc) plot final pH vs. initial pHi and (**b**) zeta potential at a function of pH.

3.2. Adsorption Experiments

Adsorption experiments were carried out at two pHs, to study the effect of pH in adsorption capacity at pH values typical of AMD waters in northern Chile. The sorption capacity q_e at different equilibrium Cu(II) concentrations (C_e) are presented graphically in Figure 5. According to experimental data, the maximum sorption capacity for Cu at pH1

(pH = 4.8) was 47.5 mg·g^{-1} (Figure 5a), reaching a maximum removal rate of 98.4% (Figure 5c), while at pH2 (pH = 4.0), the maximum sorption capacity was 40.2 mg·g^{-1} (Figure 5b) and the maximum removal rate was 93.7% (Figure 5d). Furthermore, it is possible to observe that at pH = 4.8, removal rates close to 100% are reached even at low concentrations of the metal ion, while at pH = 4.0, the sorption capacity reaches the maximum values at initial concentrations higher than 8 mg·L^{-1}. Previously, Gu et al. [85] studied the adsorption of Cu and other metals onto ZnO NPs. They reported a maximum sorption capacity of around 16 mg·g^{-1} in a multimetallic solution, where Cu is the second with more affinity with the adsorbent after Cr, which demonstrates the effectiveness of ZnO NPs for copper adsorption.
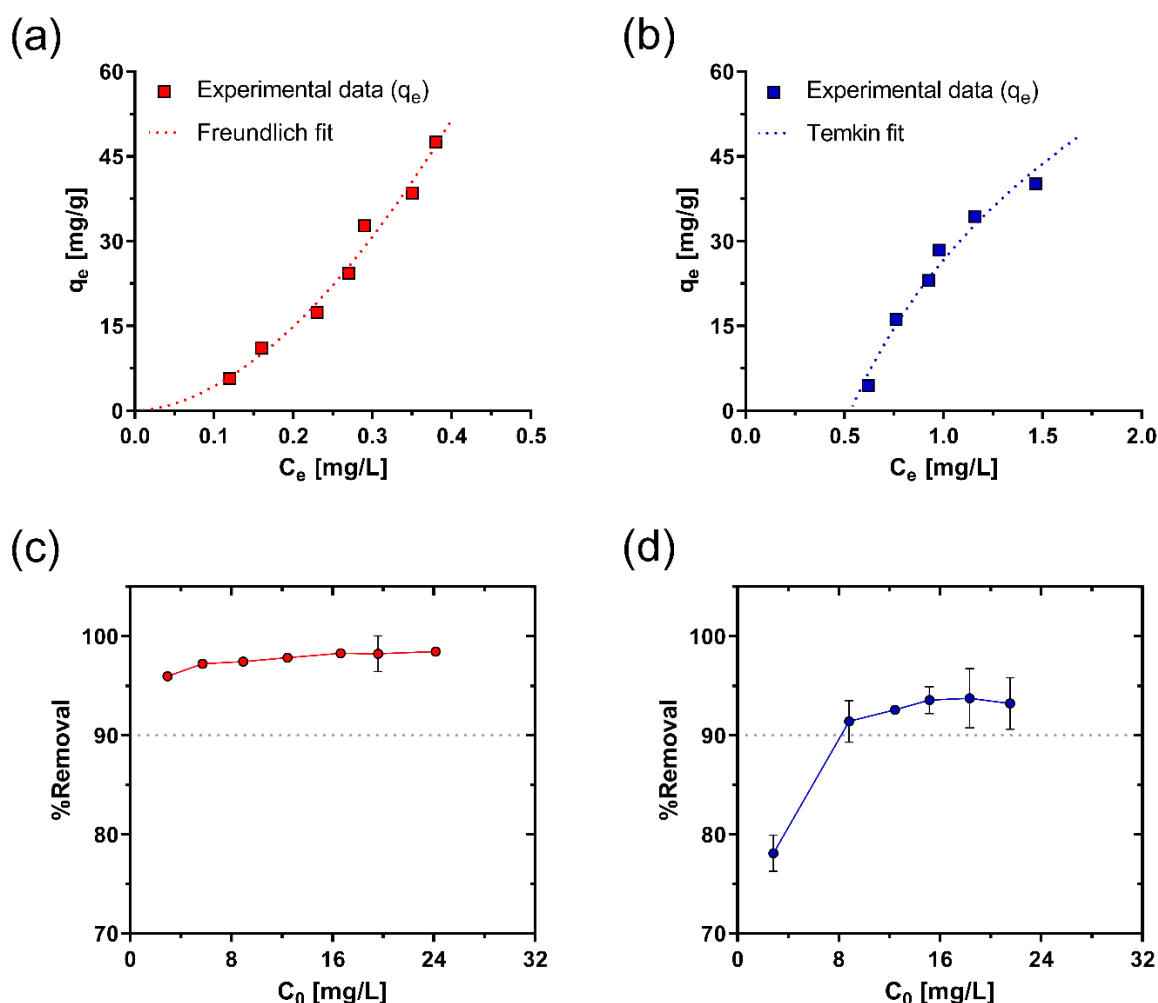

Figure 5. Adsorption isotherms for Cu(II) under (**a**) pH1 (pH = 4.8) with Freundlich isotherm model fit, and (**b**) pH2 (pH = 4.0) with Temkin isotherm model fit using ZnO NPs as nanoadsorbent. Removal percentages for Cu(II) under (**c**) pH1 (pH = 4.8) and (**d**) pH2 (pH = 4.0).

The effect of pH on the removal efficiency of Cu was studied (Appendix C). According to the results obtained, it is possible to observe that in the pH range of 4 to 10, the removal percentage was higher than 90%. At pH 2, the removal efficiency decreases considerably, reaching an average of 29%. Therefore, the removal percentage increases with increasing pH A substantial increase is observed between pH 2 and 5, and then it stabilizes around 99%, with a maximum value of 99.7% at pH 8. These results are consistent with the previous study of Yoshida [86] who observed leaching of ZnO at pH below 3. Although there are no previous studies on the effect of pH on Cu adsorption by ZnO NPs,

some studies have reported the effect of pH in the adsorption of different metals using ZnO. Sheela et al. [87] Sheela reported that the removal rates of Zn, Cd and Hg increased when the pH of the solution increased in a range of 4 to 8, and particularly, an increase between 5 and 15% in the removal rates was observed with increasing the pH from 4 to 5. Gu et al. [85] observed that the Cr adsorption capacity in ZnO NPs remained practically constant, with a slight tendency to decrease, between pH 3 and 7. The predominant factor that determines the effect of pH on adsorption corresponds to pH$_{PZC}$, which could explain the differences between the results reported by the previous studies. In our study, the pH$_{PZC}$ value for ZnO NPs was 6.21, which indicates that at a pH higher than the pH$_{PZC}$, the adsorbent surface is negatively charged, so the affinity for metal ions such as Cu is improved [88–90]. Therefore, the slight increase in adsorption capacity at higher pH observed in our study can be explained because of the pH$_{PZC}$ value.

The study carried out using multimetallic water with equal concentrations of Cu(II), Mn(II) and Al(III) shows that the removal efficiency of Cu is not affected by the presence of other ions in the solution. In the range of concentrations studied, the removal of Cu remained above 95% both in the tests carried out without pH adjustment and at pH 4.0 (Figure 6). Likewise, it is possible to observe that the ZnO NPs also showed a great affinity for the removal of Al, with removal efficiencies above 94%. Finally, Mn did not show significant adsorption on ZnO. Therefore, for the range of concentrations studied, the effect of the competition is not significant for the sorption capacity of Cu (II).
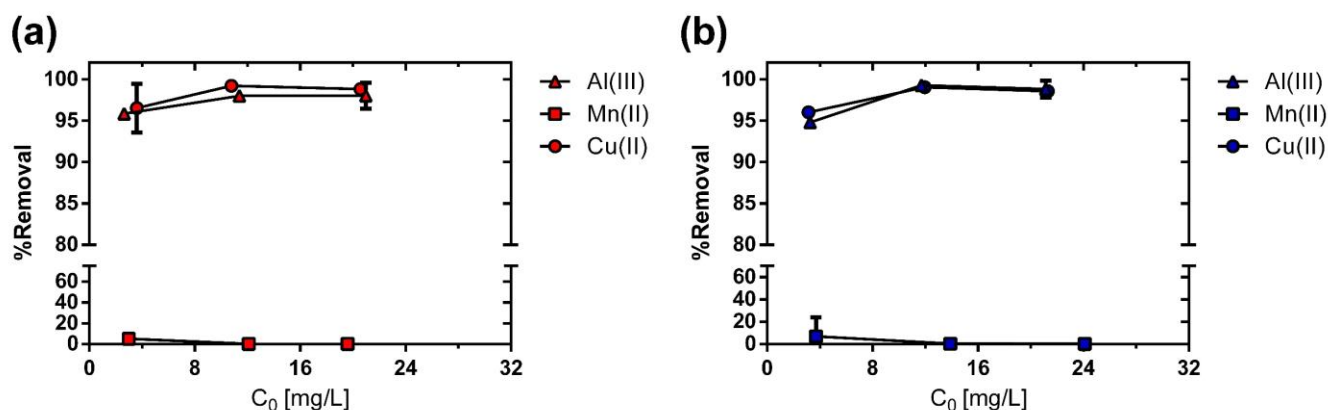

Figure 6. Removal percentages for Cu(II), Mn(II) and Al(III) under (**a**) pH1 (pH = 4.8) and (**b**) pH2 (pH = 4.0) at different initial concentrations.

Because at low pH the ZnO NPs dissolve in the aqueous solution, the desorption process is not feasible by acidifying the adsorbent medium, as has been reported for many other materials [41,91,92]. For the recovery of ZnO, it is possible to consider ultra-sonication methods to promote the desorption process and thus allow the reuse of the material. Previous studies have shown the efficiency of this method for activated carbon, among others [93–96]. There are no previous studies that account for the effectiveness of ultra-sonication for the desorption of ZnO NPs, remaining as a future perspective from this work.

SEM images of ZnO NPs at 500×, 2000×, 4000× and 5000× magnifications before adsorption of Cu(II) ions are shown in Figure 7 a–d. As seen, the ZnO NPs before contacting with Cu(II) solution are shown as clusters of aggregate particles with a rough surface and flat and irregular shapes. It has been reported that the surface energy of the photocatalyst materials, such as ZnO and TiO$_2$ NPs increases due to its smaller particle size [97]. This may support the agglomeration observed in the ZnO NPs. The specific morphologies observed in the highly porous structure of ZnO NPs support their use as nano-adsorbents for metal cations such as Cu(II) ions. Figure 7e shows the EDX spectra of ZnO NPs before

adsorption of Cu(II) ions. As seen in Figure 3c, it is observed that the atomic ratio (Zn/O) of ZnO NPs is near to 1.5:1, which confirms the chemical nature of the ZnO NPs used for the adsorption process of Cu(II) ions.
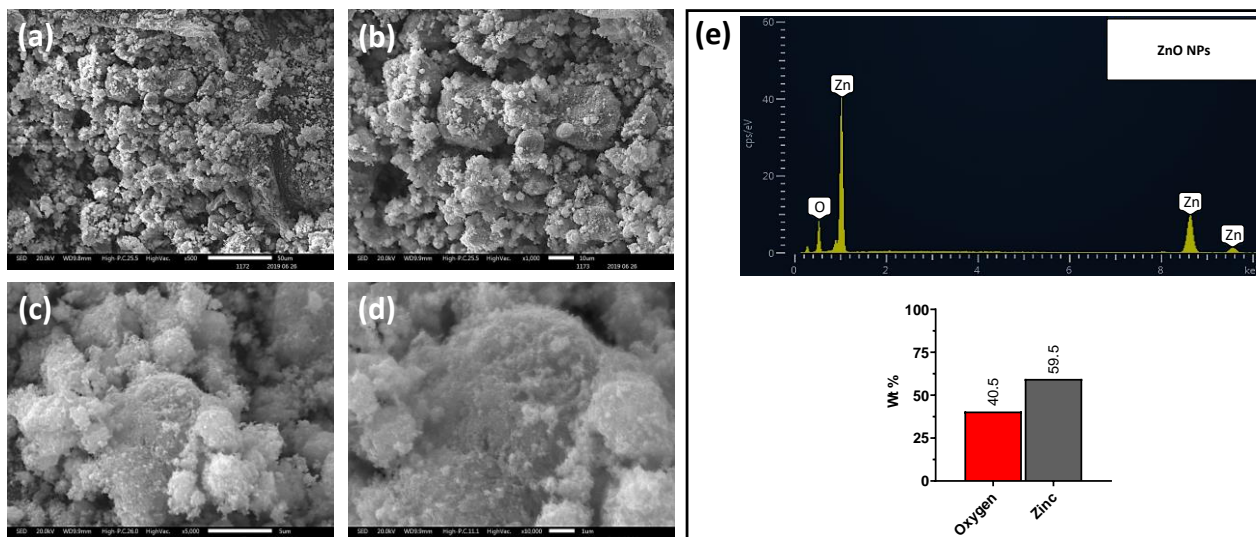

Figure 7. (**a–d**) Scanning electron micrographs before adsorption of Cu(II) ions (pH = 7.0) (**e**) SEM-EDX spectra and elemental mapping (atomic percentage %) of ZnO NPs before adsorption of Cu(II) ions. The magnifications shown in SEM images were 500× (**a**), 2000× (**b**), 4000× (**c**) and 5000× (**d**).

Figure 8 a–d shows SEM images of ZnO NP at magnifications of 500×, 1000×, 5000× and 10,000× after adsorption of Cu (II) ions. As can be seen in the SEM images, the morphology and size of ZnO NPs after reacting with the Cu(II) solution do not change significantly because of the adsorption of Cu(II) ions. The shape of ZnO NPs has no clear change after the adsorption of Cu(II) ions. This is consistent with those reported in other studies that have used ZnO NPs to adsorb metal ions such as Cr(III) [85,98]. Similarly, after adsorption of Cu (II) ions, the ZnO NPs appear to be aggregated in clusters, which occurs because of their higher surface energy. For adsorption processes, it has been observed that microporous materials (pore size < 2 nm) are more selective for adsorption and separation, while macroporous materials (pore size > 50 nm) and mesoporous materials (pore size between 2–50 nm) due to their larger pores allow different adsorbates to penetrate through them [99]. The EDX results (Figure 8e) show the adsorption of Cu(II) ions, which confirms what was seen in the adoration isotherms (Figure 5). The atomic mapping showed 2.85% weight percentage of Cu, 25.8% weight percentage of O and 71.4% weight percentage of Zn. This strongly supports the idea that Cu(II) was adsorbed onto the surface of ZnO NPs, which shows the key role these NPs play in the uptake of Cu (II) ions from AMD waters. Interestingly, the removal of Cu(II) ions by ZnO NPs are not significantly affected by acidic conditions (pH = 4.0). A remarkable aspect is the ability of ZnO NPs to maintain their structure before and after the adsorption of Cu(II) ions at acidic pH. In fact, it can be seen that the morphology of ZnO NPs does not change considerably at pH = 4 (adsorption of Cu(II) ions). Thus, this may be a key factor in promoting and scaling the use of ZnO NPs in acidic water treatment systems and metal cation removal applications. Even so, it is necessary to deepen the changes at the nanostructure level of ZnO NPs, which could be the consequence of the most aggressive acidic conditions.

To complement the adsorption analysis, the experimental data were fitted using Langmuir, Freundlich and Temkin isotherm models. The parameters for these models are summarized in Table 1. The Langmuir isotherm presented an R^2 value of 0.965 for the pH1. However, the values of the parameters q_m and K_L presented negative values, which cannot be because both parameters represent mass properties. With pH2, the coefficient of determination showed a poor fit and, again, the model parameters presented negative

values. In this way, it is ruled out that the adsorption process studied is explained by a type of monolayer adsorption [100]. For the case of pH1, the best fit corresponds to the Freundlich model, which describes multilayer adsorption onto a heterogeneous surface of the adsorbent [101–103]. Here, the stronger binding sites are occupied until the adsorption energy decreased [104]. At pH2, the model that best describes the adsorption process corresponds to the Temkin isotherm, in which is assumed that the heat of adsorption of all the molecules in the layer decreases linearly rather than logarithmically as equilibrium adsorption capacity increases [101]. Both settings are presented in Figure 5a and Figure 5b. Although the best fit model is different in the studied pH values, both have the particularity of describing a type of multilayer adsorption.
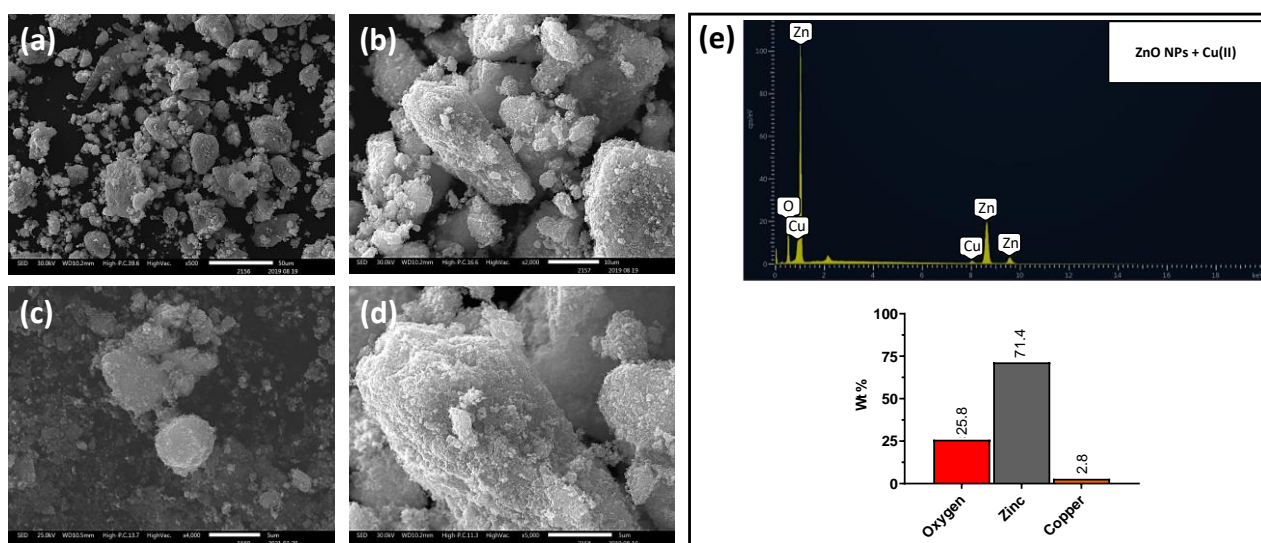

Figure 8. (**a–d**) Scanning electron micrographs after adsorption of Cu(II) ions (pH =4.0). (**e**) SEM-EDX spectra and elemental mapping (atomic percentage %) of ZnO NPs after adsorption of Cu(II) ions. The magnifications shown in SEM images were 500× (**a**), 1000× (**b**), 5000× (**c**) and 10,000× (**d**).

Table 1. Parameters for the Langmuir, Freundlich and Temkin isotherm models for Cu(II) adsorption performed under two pHs.

pH	Nano-Adsorbent	Langmuir			Freundlich			Temkin		
		q_m (mg·g^{-1})	K_L (L·mg^{-1})	R^2	K_F (L·g^{-1})	n	R^2	K_T (L·g^{-1})	B_T (mg·L^{-1})	R^2
pH 4.8	ZnO	−18.28	−2.1	0.965	264.85	0.56	0.988	8.69	34.45	0.908
pH 4.0	ZnO	−6.64	−0.75	0.739	22.75	0.42	0.830	1.89	41.98	0.975

At pH values lower than 5, the dominant copper species is its divalent form Cu(II) and in the pH range studied in this work (4.0–4.8), copper speciation should be similar in both pHs [30,105]. Although the differences in the sorption capacity between the two pHs are slight, the differences are mainly explained by the surface charge of the ZnO NPs as a function of the pH$_{PZC}$ value. In this way, the chemical interaction between the functional groups of the NPs and Cu(II) could explain the adsorption mechanism. Although both pH values are below the pH$_{PZC}$, and yet the removal rates obtained were close to 100%, it is possible to deduce that physical adsorption plays an important role in the adsorption mechanism. This can also be confirmed by the high BET surface area value found for ZnO NPs (45.58 m²·g^{-1}, Figure 2), which may support the idea that physical adsorption is the dominant mechanism overcoming the repulsions generated by being below the pH$_{PZC}$.

The thermodynamic parameter ΔG^0 was determined using the equilibrium constant obtained from Temkin and Freundlich fit for the experiments with and without adjusting

pH, respectively since these isotherm models presented a better fit for each case. The results are presented in Table 2. According to the values obtained, the adsorption test at pH 4.8 presented a higher negative value than in the case at pH 4, so that at a higher pH the adsorption process is energetically more favorable.

Table 2. Gibbs free energy (ΔG^0) for adsorption processes under two pHs.

pH	K (L·g^{-1})	ΔG^0 (kJ·mol^{-1})
pH 4.8	264.85	−13,829.74
pH 4.0	1.89	−1577.96

3.3. Surface Analysis: Roughness

To analyze changes at the nanostructure level of the ZnO NPs before and after reacting with Cu(II) solution, SEM images and their corresponding 3D surface profiles were determined through image Gwyddion software. SEM images are directly related to their real relief and therefore these images can be used to determine changes in the surface roughness of a specific material. Likewise, changes in roughness can be the consequence of chemical reactions on the surfaces of ZnO NPs. In this way, these analyzes can provide quantitative data on changes in surface roughness because of the effect of chemical adsorption conditions or interactions with specific adsorbates. Figure 9 shows 3D images of the ZnO NP before (Figure 9a) and after (Figure 9b) adsorption of Cu(II) ions. It is clearly observed that the surface roughness of ZnO NPs prior to the adsorption of Cu(II) ions is greater than after contacting the Cu(II) solution at pH = 4.0. This can be a consequence of more aggressive pH conditions that wear away the nano-adsorbent surface (ZnO NPs).

For quantitative analysis, the surface roughness parameters R_a, R_q, R_{sk} and R_{ku} were obtained by the Gwyddion software (Figure 9a,b). The R_a values of ZnO NPs before adsorption of Cu(II) ions shows an average value of 29.997 ± 8.663, while R_a values of ZnO NPs after adsorption of Cu(II) ions shows an average value of 9.348 ± 1.281, evidencing a marked decrease in surface roughness by approximately 70%. This shows that more aggressive acidic conditions (pH = 4.0) can produce changes at the nanostructural level, although these changes are not evident in changes in the morphology, shape, and particle size of the ZnO NPs. The R_q of ZnO NPs before and after adsorption Cu(II) ion were 37.920 ± 11.077 and 11.877 ± 1.690, respectively. This shows that surface roughness variation in ZnO NPs before adsorption of Cu(II) ions is higher than that in ZnO NPs after adsorption of Cu(II) ions, which suggests that acidic solutions enriched in Cu(II) can homogenize the surface of the ZnO NPs. The R_{sk} values were very similar for the samples of ZnO NPs before and after the adsorption of Cu(II) ions. Even so, the R_{sk} values were positive for ZnO NPs before the adsorption of Cu(II) ions, which shows that in these samples there are more troughs than peaks on the surface. On the contrary, R_{sk} values were negative for ZnO NPs after adsorption of Cu(II) ions, showing that in these samples that there are fewer troughs than peaks. Finally, the R_{ku} values were similar for both conditions, before (3.344 ± 0.284) and after (3.232 ± 0.213) the adsorption of Cu(II) ions. This shows that the shape of the pore size distribution is concentrated in both conditions. It has been observed that the joint strength between adhesive and adherent is influenced by the surface roughness of the adherents [106]. Therefore, the surface roughness of the nano-adsorbent (e.g., ZnO NPs) could also be critical for adsorbate–adsorbent interactions.
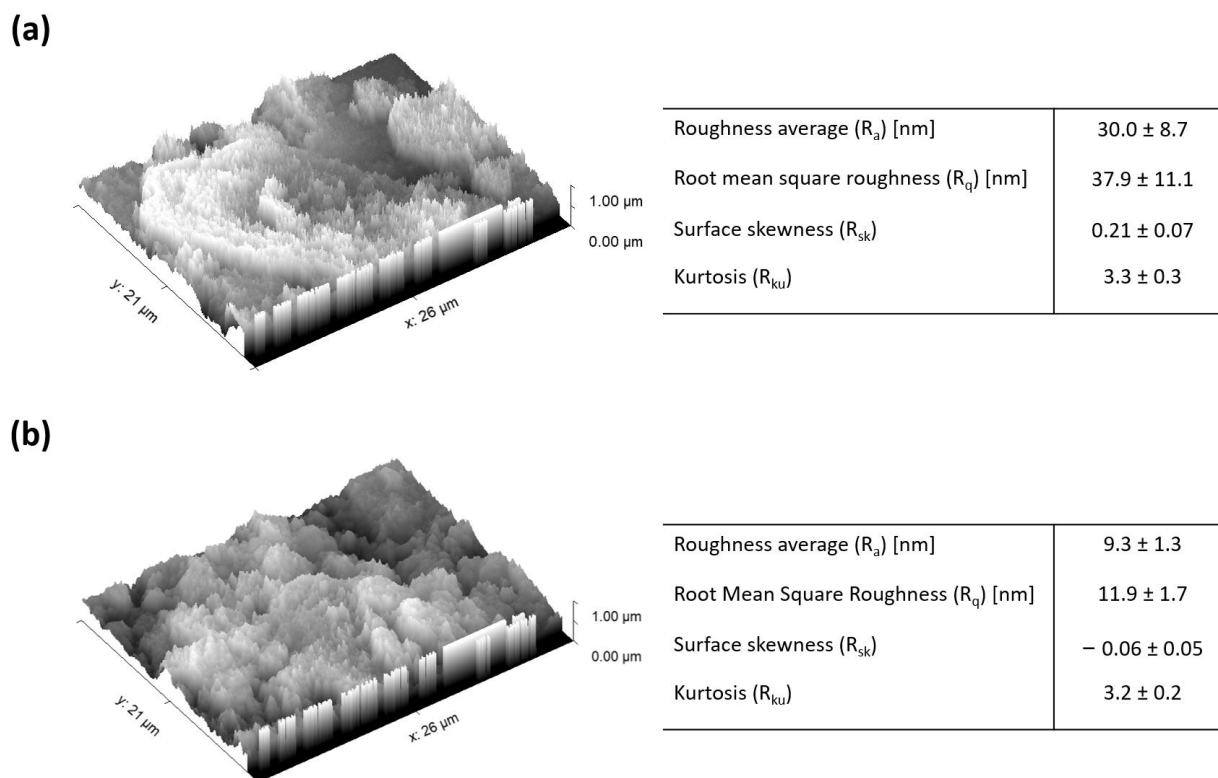
(a)

Roughness average (R$_a$) [nm]	30.0 ± 8.7
Root mean square roughness (R$_q$) [nm]	37.9 ± 11.1
Surface skewness (R$_{sk}$)	0.21 ± 0.07
Kurtosis (R$_{ku}$)	3.3 ± 0.3

(b)

Roughness average (R$_a$) [nm]	9.3 ± 1.3
Root Mean Square Roughness (R$_q$) [nm]	11.9 ± 1.7
Surface skewness (R$_{sk}$)	− 0.06 ± 0.05
Kurtosis (R$_{ku}$)	3.2 ± 0.2

Figure 9. 3-D SEM images and surface roughness parameters of ZnO NPs before (**a**) and after (**b**) Cu(II) adsorption. The 3-D SEM images and surface roughness parameters (*Ra, Rq, Rsk* and *Rku*) were obtained by the Gwyddion software.

3.4. Kinetic Studies of the Adsorption

The study of the adsorption kinetics showed that after 240 min of contact time, removal of over 90% of Cu(II) is achieved (Figure 10). The experimental data were fitted with pseudo-first-order and pseudo-second-order kinetic models. Table 3 summarizes the kinetic parameters obtained for both models. According to R^2 and q_e values, it could be determined that the pseudo-second-order presented a better fit. The pseudo-second-order describes a sorption process mainly controlled by the adsorption reaction at the liquid/solid interface at the adsorbent, in contrast to the pseudo-first-order model, which describes a diffusion-controlled process [41,107]. Previous studies about the use of ZnO NPs for the adsorption of different pollutants, such as Zn, Cd, Hg, Cr, among others, have shown that the pseudo-second-order model is the one that best adjusts to the adsorption kinetics [85,87,108,109]. The approaching equilibrium factor (*Rw*) obtained was 0.024, which is related to a type of kinetic curve largely curved. This value also shows a well-approaching equilibrium level [69].

Table 3. Kinetic adsorption parameters for pseudo-first-order and pseudo-second-order models.

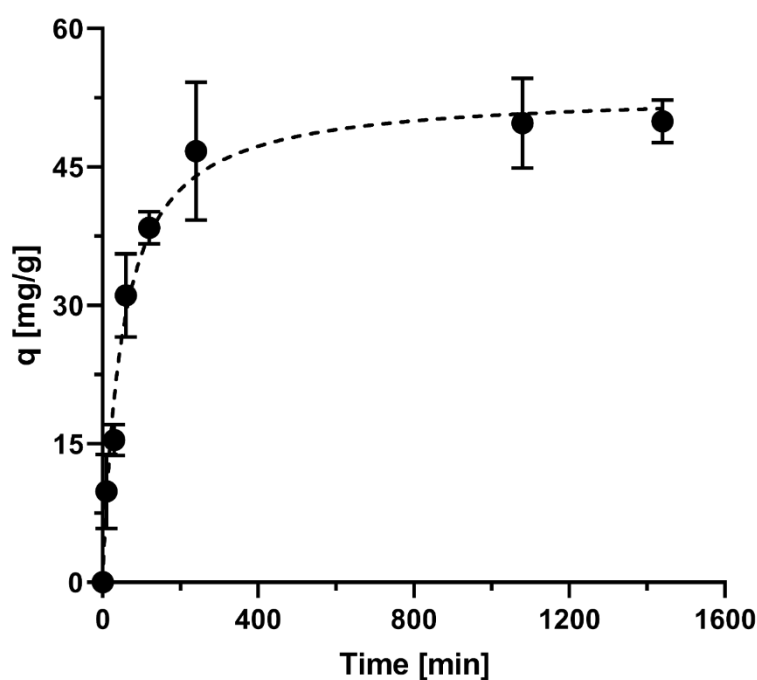| Nano-Adsorbent	q_e^{exp} (mg·g^{-1})	Pseudo-First-Order			Pseudo-Second-Order		
		k_1 (1·min^{-1})	q_{e1} (mg·g^{-1})	R^2	k_2 (g·mg^{-1} min^{-1})	q_{e2} (mg·g^{-1})	R^2
ZnO	49.94	0.011	28.94	0.922	0.0054	51.28	0.999

Figure 10. Effect of contact time on removal Cu(II) ions. The kinetic curve for Cu(II) is based on the pseudo-second-order model.

4. Conclusions

The results show that ZnO NPs have a great affinity for Cu(II) ions, getting adsorption capacities even higher than previous studies. The characterization analyzes of the nano-adsorbent allowed us to observe that the ZnO NPs form agglomerations, which could decrease the total surface area and give an underestimated result of this value through the BET analysis. Raman confirmed the presence of ZnO NPs and SEM-EDX and FESEM confirmed that the ZnO NPs are of nano size (<100 nm).

The study of different pHs demonstrates that even though large variations in adsorption capacity do not occur when the pH varies between 4.0 and 4.8, a slight improvement is observed at pH 4.8, which is mainly explained by the value of pH$_{PZC}$ of the nano-adsorbent, corresponding to 6.21. It is expected that, at pH values higher than pH$_{PZC}$, the adsorption capacity will be even higher. In addition, it is possible to observe that at pH 4.8 the removal rate is higher at low concentrations than at pH 4. The results suggest that the adsorption process occurs by a physical mechanism rather than by chemical adsorption since at the evaluated pHs there are higher repulsions than attraction forces on the surface of ZnO NPs. Likewise, the surface roughness analysis showed a marked decrease in surface roughness of ZnO NPs by approximately 70% after adsorption of Cu(II) ions at pH 4.0, which shows that more acidic conditions can produce changes at the nanostructural level. Although these changes are not clear in the changes in the morphology, shape, particle size of the ZnO NPs and in the removal rates of Cu(II) ions. Adjustments with isotherm models allowed determining that adsorption occurs mainly because of the formation of multi-layers on the surface of the ZnO NPs. The kinetics showed that the pseudo-second-order model better fit the experimental data.

These findings contribute to a better understanding of the adsorption of Cu metal ions onto ZnO NPs and the effect of slight variations in pHs. However, additional efforts are necessary to improve the knowledge of the effect of pH under more extreme conditions and considering multimetallic waters that represent a more realistic scenario in the composition of AMD characteristic waters.

Appendix A

Table A1. Costs of wastewater treatment technologies.

Technology	Cost per Million Liters	Reference
Adsorption	USD 10 to 200 USD 50 to 150	[28,29]
Ion Exchange	USD 50 to 200	[29]
Reverse Osmosis	USD 200 to 450	[29]
Micro- and ultra-filtration	USD 15 to 400	[29]
Electrodialysis	USD 15 to 400	[29]

Appendix B

Table A2. Costs of nanomaterials for adsorption treatment technologies.

Nanomaterial	Cost per Gram	Reference
ZnO nanoparticles	USD 7.6	[110]
Graphene	USD 632.73	[111]
Carbon nanotubes	USD 263	[112]

Appendix C

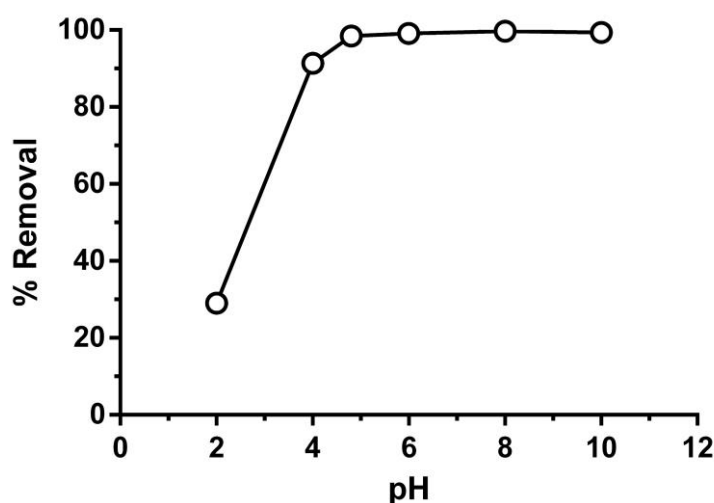**Figure A1.** Effect of pH on Cu(II) ions removal. The initial concentration was 24 mg·L^{-1} in each case.

References

1. Blowes, D.W.; Ptacek, C.J.; Jambor, J.L.; Weisener, C.G. The Geochemistry of Acid Mine Drainage. In *Treatise on Geochemistry*; Elsevier Inc.: Amsterdam, The Netherlands, 2003; Volume 9–9, pp. 149–204. ISBN 9780080548074.
2. Naidu, G.; Ryu, S.; Thiruvenkatachari, R.; Choi, Y.; Jeong, S.; Vigneswaran, S. A critical review on remediation, reuse, and resource recovery from acid mine drainage. *Environ. Pollut.* **2019**, *247*, 1110–1124.
3. Kefeni, K.K.; Msagati, T.A.M.; Mamba, B.B. Acid mine drainage: Prevention, treatment options, and resource recovery: A review. *J. Clean. Prod.* **2017**, *151*, 475–493.
4. Akcil, A.; Koldas, S. Acid Mine Drainage (AMD): Causes, treatment and case studies. *J. Clean. Prod.* **2006**, *14*, 1139–1145.
5. Carolin, C.F.; Kumar, P.S.; Saravanan, A.; Joshiba, G.J.; Naushad, M. Efficient techniques for the removal of toxic heavy metals from aquatic environment: A review. *J. Environ. Chem. Eng.* **2017**, *5*, 2782–2799.
6. Vardhan, K.H.; Kumar, P.S.; Panda, R.C. A review on heavy metal pollution, toxicity and remedial measures: Current trends and future perspectives. *J. Mol. Liq.* **2019**, *290*, 111197.
7. Visa, M. Synthesis and characterization of new zeolite materials obtained from fly ash for heavy metals removal in advanced wastewater treatment. *Powder Technol.* **2016**, *294*, 338–347.
8. Malik, A. Metal bioremediation through growing cells. *Environ. Int.* **2004**, *30*, 261–278.
9. Ziagova, M.; Dimitriadis, G.; Aslanidou, D.; Papaioannou, X.; Litopoulou Tzannetaki, E.; Liakopoulou-Kyriakides, M. Comparative study of Cd(II) and Cr(VI) biosorption on Staphylococcus xylosus and Pseudomonas sp. in single and binary mixtures. *Bioresour. Technol.* **2007**, *98*, 2859–2865.
10. Chouyyok, W.; Shin, Y.; Davidson, J.; Samuels, W.D.; Lafemina, N.H.; Rutledge, R.D.; Fryxell, G.E.; Sangvanich, T.; Yantasee, W. Selective removal of copper(II) from natural waters by nanoporous sorbents functionalized with chelating diamines. *Environ. Sci. Technol.* **2010**, *44*, 6390–6395.
11. Akbari, M.; Hallajisani, A.; Keshtkar, A.R.; Shahbeig, H.; Ali Ghorbanian, S. Equilibrium and kinetic study and modeling of Cu(II) and Co(II) synergistic biosorption from Cu(II)-Co(II) single and binary mixtures on brown algae C. indica. *J. Environ. Chem. Eng.* **2015**, *3*, 140–149.
12. Ahmad, A.; Rafatullah, M.; Sulaiman, O.; Ibrahim, M.H.; Chii, Y.Y.; Siddique, B.M. Removal of Cu(II) and Pb(II) ions from aqueous solutions by adsorption on sawdust of Meranti wood. *Desalination* **2009**, *247*, 636–646.
13. Stylianou, M.A.; Inglezakis, V.J.; Moustakas, K.G.; Malamis, S.P.; Loizidou, M.D. Removal of Cu(II) in fixed bed and batch reactors using natural zeolite and exfoliated vermiculite as adsorbents. *Desalination* **2007**, *215*, 133–142.
14. Salomons, W. Environmental impact of metals derived from mining activities: Processes, predictions, prevention. *J. Geochem. Explor.* **1995**, *52*, 5–23.
15. Rodríguez, C.; Leiva-Aravena, E.; Serrano, J.; Leiva, E. Occurrence and removal of copper and aluminum in a stream confluence affected by acid mine drainage. *Water* **2018**, *10*, 516.
16. Al-Saydeh, S.A.; El-Naas, M.H.; Zaidi, S.J. Copper removal from industrial wastewater: A comprehensive review. *J. Ind. Eng. Chem.* **2017**, *56*, 35–44.
17. Andrejkovičová, S.; Sudagar, A.; Rocha, J.; Patinha, C.; Hajjaji, W.; Da Silva, E.F.; Velosa, A.; Rocha, F. The effect of natural zeolite on microstructure, mechanical and heavy metals adsorption properties of metakaolin based geopolymers. *Appl. Clay Sci.* **2016**, *126*, 141–152.

18. Satyro, S.; Marotta, R.; Clarizia, L.; Di Somma, I.; Vitiello, G.; Dezotti, M.; Pinto, G.; Dantas, R.F.; Andreozzi, R. Removal of EDDS and copper from waters by TiO2 photocatalysis under simulated UV-solar conditions. *Chem. Eng. J.* **2014**, *251*, 257–268.

19. Li, X.; Deng, G.; Zhang, Y.; Wang, J. Rapid removal of copper ions from aqueous media by hollow polymer nanoparticles. *Colloids Surf. A Physicochem. Eng. Asp.* **2019**, *568*, 345–355.

20. Matouq, M.; Jildeh, N.; Qtaishat, M.; Hindiyeh, M.; Al Syouf, M.Q. The adsorption kinetics and modeling for heavy metals removal from wastewater by Moringa pods. *J. Environ. Chem. Eng.* **2015**, *3*, 775–784.

21. Wang, X.; Yu, S.; Jin, J.; Wang, H.; Alharbi, N.S.; Alsaedi, A.; Hayat, T.; Wang, X. Application of graphene oxides and graphene oxide-based nanomaterials in radionuclide removal from aqueous solutions. *Sci. Bull.* **2016**, *61*, 1583–1593.

22. Gros, F.; Baup, S.; Aurousseau, M. Copper cementation on zinc and iron mixtures: Part 1: Results on rotating disc electrode. *Hydrometallurgy* **2011**, *106*, 119–126.

23. Ferrer, O.; Gibert, O.; Cortina, J.L. Reverse osmosis membrane composition, structure and performance modification by bisulphite, iron(III), bromide and chlorite exposure. *Water Res.* **2016**, *103*, 256–263.

24. Xu, Y.C.; Wang, Z.X.; Cheng, X.Q.; Xiao, Y.C.; Shao, L. Positively charged nanofiltration membranes via economically mussel-substance-simulated co-deposition for textile wastewater treatment. *Chem. Eng. J.* **2016**, *303*, 555–564.

25. Caprarescu, S.; Corobea, M.C.; Purcar, V.; Spataru, C.I.; Ianchis, R.; Vasilievici, G.; Vuluga, Z. San copolymer membranes with ion exchangers for Cu(II) removal from synthetic wastewater by electrodialysis. *J. Environ. Sci.* **2015**, *35*, 27–37.

26. Dong, Y.; Liu, J.; Sui, M.; Qu, Y.; Ambuchi, J.J.; Wang, H.; Feng, Y. A combined microbial desalination cell and electrodialysis system for copper-containing wastewater treatment and high-salinity-water desalination. *J. Hazard. Mater.* **2017**, *321*, 307–315.

27. Kanakaraju, D.; Ravichandar, S.; Lim, Y.C. Combined effects of adsorption and photocatalysis by hybrid TiO2/ZnO-calcium alginate beads for the removal of copper. *J. Environ. Sci.* **2017**, *55*, 214–223.

28. Ali, I.; Gupta, V.K. Advances in water treatment by adsorption technology. *Nat. Protoc.* **2007**, *1*, 2661–2667.

29. Gupta, V.K.; Ali, I.; Saleh, T.A.; Nayak, A.; Agarwal, S. Chemical treatment technologies for waste-water recycling—An overview. *RSC Adv.* **2012**, *2*, 6380–6388.

30. Demiral, H.; Güngör, C. Adsorption of copper(II) from aqueous solutions on activated carbon prepared from grape bagasse. *J. Clean. Prod.* **2016**, *124*, 103–113.

31. Yang, S.T.; Chang, Y.; Wang, H.; Liu, G.; Chen, S.; Wang, Y.; Liu, Y.; Cao, A. Folding/aggregation of graphene oxide and its application in Cu2+ removal. *J. Colloid Interface Sci.* **2010**, *351*, 122–127.

32. Bansode, R.R.; Losso, J.N.; Marshall, W.E.; Rao, R.M.; Portier, R.J. Adsorption of metal ions by pecan shell-based granular activated carbons. *Bioresour. Technol.* **2003**, *89*, 115–119.

33. Lee, S.M.; Davis, A.P. Removal of cu(II) and cd(II) from aqueous solution by seafood processing waste sludge. *Water Res.* **2001**, *35*, 534–540.

34. Sitko, R.; Turek, E.; Zawisza, B.; Malicka, E.; Talik, E.; Heimann, J.; Gagor, A.; Feist, B.; Wrzalik, R. Adsorption of divalent metal ions from aqueous solutions using graphene oxide. *Dalton Trans.* **2013**, *42*, 5682–5689.

35. Abou-Zeid, R.E.; Dacrory, S.; Ali, K.A.; Kamel, S. Novel method of preparation of tricarboxylic cellulose nanofiber for efficient removal of heavy metal ions from aqueous solution. *Int. J. Biol. Macromol.* **2018**, *119*, 207–214.

36. Mautner, A.; Maples, H.A.; Kobkeatthawin, T.; Kokol, V.; Karim, Z.; Li, K.; Bismarck, A. Phosphorylated nanocellulose papers for copper adsorption from aqueous solutions. *Int. J. Environ. Sci. Technol.* **2016**, *13*, 1861–1872.

37. Cegłowski, M.; Gierczyk, B.; Frankowski, M.; Popenda, Ł. A new low-cost polymeric adsorbents with polyamine chelating groups for efficient removal of heavy metal ions from water solutions. *React. Funct. Polym.* **2018**, *131*, 64–74.

38. Karami, S.; Zeynizadeh, B. Reduction of 4-nitrophenol by a disused adsorbent: EDA-functionalized magnetic cellulose nanocomposite after the removal of Cu 2+. *Carbohydr. Polym.* **2019**, *211*, 298–307.

39. Liu, F.; Zhou, K.; Chen, Q.; Wang, A.; Chen, W. Application of magnetic ferrite nanoparticles for removal of Cu(II) from copper-ammonia wastewater. *J. Alloys Compd.* **2019**, *773*, 140–149.

40. Salam, M.A. Removal of heavy metal ions from aqueous solutions with multi-walled carbon nanotubes: Kinetic and thermodynamic studies. *Int. J. Environ. Sci. Technol.* **2013**, *10*, 677–688.

41. Rodríguez, C.; Leiva, E. Enhanced heavy metal removal from acid mine drainage wastewater using double-oxidized multi-walled carbon nanotubes. *Molecules* **2019**, *25*, 111.

42. Rodríguez, C.; Briano, S.; Leiva, E. Increased adsorption of heavy metal ions in multi-walled carbon nanotubes with improved dispersion stability. *Molecules* **2020**, *25*, 3106.

43. Abuhatab, S.; El-Qanni, A.; Al-Qalaq, H.; Hmoudah, M.; Al-Zerei, W. Effective adsorptive removal of Zn2+, Cu2+, and Cr3+ heavy metals from aqueous solutions using silica-based embedded with NiO and MgO nanoparticles. *J. Environ. Manag.* **2020**, *268*, 110713.

44. Li, S.; Wang, W.; Liang, F.; Zhang, W.X. Heavy metal removal using nanoscale zero-valent iron (nZVI): Theory and application. *J. Hazard. Mater.* **2017**, *322*, 163–171.

45. Tan, P.; Sun, J.; Hu, Y.; Fang, Z.; Bi, Q.; Chen, Y.; Cheng, J. Adsorption of Cu2+, Cd2+ and Ni2+ from aqueous single metal solutions on graphene oxide membranes. *J. Hazard. Mater.* **2015**, *297*, 251–260.

46. Salahuddin, N.; El-Kemary, M.; Ibrahim, E.M. Synthesis and characterization of ZnO nanoparticles via precipitation method: Effect of annealing temperature on particle size. *Nanosci. Nanotechnol.* **2015**, *5*, 82–88.

47. Ruszkiewicz, J.A.; Pinkas, A.; Ferrer, B.; Peres, T.V.; Tsatsakis, A.; Aschnera, M. Neurotoxic effect of active ingredients in sunscreen products, a contemporary review. *Toxicol. Rep.* **2017**, *4*, 245–259.

48. Siddiqi, K.S.; Rahman, A.U.; Tajuddin, H.A. Properties of zinc oxide nanoparticles and their activity against microbes. *Nanoscale Res. Lett.* **2018**, *13*, 1–13.
49. Sawai, J. Quantitative evaluation of antibacterial activities of metallic oxide powders (ZnO, MgO and CaO) by conductimetric assay. *J. Microbiol. Methods* **2003**, *54*, 177–182.
50. Chen, C.C.; Liu, P.; Lu, C.H. Synthesis and characterization of nano-sized ZnO powders by direct precipitation method. *Chem. Eng. J.* **2008**, *144*, 509–513.
51. Li, Y.; Lu, X.; Qi, H.; Li, X.; Xiao, X.; Gao, J. Ursolic acid induces apoptosis through mitochondrial intrinsic pathwayand suppression of ERK1/2 MAPK in HeLa cells. *J. Pharmacol. Sci.* **2014**, *125*, 202–210.
52. Qamar, M.; Gondal, M.A.; Yamani, Z.H. Laser-induced efficient reduction of Cr(VI) catalyzed by ZnO nanoparticles. *J. Hazard. Mater.* **2011**, *187*, 258–263.
53. Chakrabarti, S.; Chaudhuri, B.; Bhattacharjee, S.; Ray, A.K.; Dutta, B.K. Photo-reduction of hexavalent chromium in aqueous solution in the presence of zinc oxide as semiconductor catalyst. *Chem. Eng. J.* **2009**, *153*, 86–93.
54. Shirzad-Siboni, M.; Farrokhi, M.; Darvishi Cheshmeh Soltani, R.; Khataee, A.; Tajassosi, S. Photocatalytic reduction of hexavalent chromium over ZnO nanorods immobilized on kaolin. *Ind. Eng. Chem. Res.* **2014**, *53*, 1079–1087.
55. Siboni, M.S.; Samadi, M.T.; Yang, J.K.; Lee, S.M. Photocatalytic reduction of Cr(VI) and Ni(II) in aqueous solution by synthesized nanoparticle ZnO under ultraviolet light irradiation: A kinetic study. *Environ. Technol.* **2011**, *32*, 1573–1579.
56. Lee, J.H.; Seo, J.U.; Chung, Y.J.; Lee, J.C.; Park, S. Removal of heavy metal ions from aqueous Pb-EDTA and Cu-EDTA solutions using nanosized ZnO powders by solution-combustion method. *Key Eng. Mater.* **2006**, *317–318*, 837–840.
57. Lee, J.C.; Kim, H.S.; Lee, J.H.; Park, S. Photocatalytic removal of Cu ions from aqueous Cu-EDTA solution using solution combusted zinc oxide nanopowder. *J. Nanosci. Nanotechnol.* **2008**, *8*, 5284–5287.
58. Le, A.T.; Pung, S.Y.; Sreekantan, S.; Matsuda, A.; Huynh, D.P. Mechanisms of removal of heavy metal ions by ZnO particles. *Heliyon* **2019**, *5*, e01440.
59. Wang, X.; Cai, W.; Liu, S.; Wang, G.; Wu, Z.; Zhao, H. ZnO hollow microspheres with exposed porous nanosheets surface: Structurally enhanced adsorption towards heavy metal ions. *Colloids Surf. A Physicochem. Eng. Asp.* **2013**, *422*, 199–205.
60. De Primo, J.O.; Bittencourt, C.; Acosta, S.; Sierra-Castillo, A.; Colomer, J.-F.; Jaerger, S.; Teixeira, V.C.; Anaissi, F.J. Synthesis of zinc oxide nanoparticles by ecofriendly routes: Adsorbent for copper removal from wastewater. *Front. Chem.* **2020**, *8*, 1100.
61. Pashai Gatabi, M.; Milani Moghaddam, H.; Ghorbani, M. Point of zero charge of maghemite decorated multiwalled carbon nanotubes fabricated by chemical precipitation method. *J. Mol. Liq.* **2016**, *216*, 117–125.
62. Vasconcelos, H.L.; Camargo, T.P.; Gonçalves, N.S.; Neves, A.; Laranjeira, M.C.M.; Fávere, V.T. Chitosan crosslinked with a metal complexing agent: Synthesis, characterization and copper(II) ions adsorption. *React. Funct. Polym.* **2008**, *68*, 572–579.
63. Langmuir, I. The constitution and fundamental properties of solids and liquids. II. Liquids. *J. Am. Chem. Soc.* **1917**, *39*, 1848–1906.
64. Freundlich, H.M.F. Over the adsorption in solution. *J. Phys. Chem* **1906**, *57*, 1100–1107.
65. Vaghetti, J.C.P.; Lima, E.C.; Royer, B.; da Cunha, B.M.; Cardoso, N.F.; Brasil, J.L.; Dias, S.L.P. Pecan nutshell as biosorbent to remove Cu(II), Mn(II) and Pb(II) from aqueous solutions. *J. Hazard. Mater.* **2009**, *162*, 270–280.
66. Tempkin, M.I.; Pyzhev, V. Kinetics of ammonia synthesis on promoted iron catalyst. *Acta Phys. Chim. USSR* **1940**, *12*, 327.
67. Nečas, D.; Klapetek, P. Gwyddion: An open-source software for SPM data analysis. *Open Phys.* **2012**, *10*, 181–188.
68. Zhao, S.; Li, Y.; Wang, Y.; Ma, Z.; Huang, X. Quantitative study on coal and shale pore structure and surface roughness based on atomic force microscopy and image processing. *Fuel* **2019**, *244*, 78–90.
69. Ding, P.; Huang, K.L.; Li, G.Y.; Zeng, W.W. Mechanisms and kinetics of chelating reaction between novel chitosan derivatives and Zn(II). *J. Hazard. Mater.* **2007**, *146*, 58–64.
70. Ho, Y.S.; McKay, G. Comparative sorption kinetic studies of dye and aromatic compounds onto fly ash. *J. Environ. Sci. Heal. Part A Toxic/Hazard. Subst. Environ. Eng.* **1999**, *34*, 1179–1204.
71. Wu, F.C.; Tseng, R.L.; Huang, S.C.; Juang, R.S. Characteristics of pseudo-second-order kinetic model for liquid-phase adsorption: A mini-review. *Chem. Eng. J.* **2009**, *151*, 1–9.
72. Jia, C.S.; Zhang, L.H.; Peng, X.L.; Luo, J.X.; Zhao, Y.L.; Liu, J.Y.; Guo, J.J.; Tang, L.D. Prediction of entropy and Gibbs free energy for nitrogen. *Chem. Eng. Sci.* **2019**, *202*, 70–74.
73. Özcan, A.; Özcan, A.S.; Tunali, S.; Akar, T.; Kiran, I. Determination of the equilibrium, kinetic and thermodynamic parameters of adsorption of copper(II) ions onto seeds of Capsicum annuum. *J. Hazard. Mater.* **2005**, *124*, 200–208.
74. Aksu, Z. Determination of the equilibrium, kinetic and thermodynamic parameters of the batch biosorption of nickel(II) ions onto Chlorella vulgaris. *Process Biochem.* **2002**, *38*, 89–99.
75. Arguello, C.A.; Rousseau, D.L.; Porto, S.P.S. First-Order Raman Effect in Wurtzite-Type Crystals. *Phys. Rev.* **1969**, *181*, 1351.
76. Ristić-Djurović, J.L.; Fernández-Izquierdo, L.; Hadžić, B.; Jiménez-Hernández, L.; Díaz-García, A.M.; Mitrić, J.; Babić, B.; Romčević, M.; Ćirković, S.; Romčević, N. Raman spectroscopy of zinc oxide nanoplatelets modified with ruthenium (II) complexes. *J. Raman Spectrosc.* **2019**, *50*, 1829–1838.
77. Cuscó, R.; Alarcón-Lladó, E.; Ibanez, J.; Artús, L.; Jiménez, J.; Wang, B.; Callahan, M.J. Temperature dependence of Raman scattering in ZnO. *Phys. Rev. B* **2007**, *75*, 165202.
78. Zafar, M.N.; Dar, Q.; Nawaz, F.; Zafar, M.N.; Iqbal, M.; Nazar, M.F. Effective adsorptive removal of azo dyes over spherical ZnO nanoparticles. *J. Mater. Res. Technol.* **2019**, *8*, 713–725.

79. Kataria, N.; Garg, V.K. Removal of Congo red and Brilliant green dyes from aqueous solution using flower shaped ZnO nano-particles. *J. Environ. Chem. Eng.* **2017**, *5*, 5420–5428.

80. Chauhan, A.K.; Kataria, N.; Garg, V.K. Green fabrication of ZnO nanoparticles using Eucalyptus spp. leaves extract and their application in wastewater remediation. *Chemosphere* **2020**, *247*, 125803.

81. Kragović, M.; Stojmenović, M.; Petrović, J.; Loredo, J.; Pašalić, S.; Nedeljković, A.; Ristović, I. Influence of alginate encapsulation on point of zero charge (pH pzc) and thermodynamic properties of the natural and Fe(III)-modified zeolite. *Procedia Manuf.* **2019**, *32*, 286–293.

82. Zhao, T.; Fang, M.; Tang, Z.; Zhao, X.; Wu, F. Adsorption, aggregation and sedimentation of titanium dioxide nanoparticles and nanotubes in the presence of different sources of humic acids. *Sci. Total Environ.* **2019**, *692*, 660–668.

83. Alvarez-Silva, M.; Mirnezami, M.; Uribe-Salas, A.; Finch, J.A. Point of zero charge, isoelectric point and aggregation of phyllo-silicate minerals. *Can. J. Metall. Mater. Sci.* **2013**, *49*, 405–410.

84. Suttiponparnit, K.; Jiang, J.; Sahu, M.; Suvachittanont, S.; Charinpanitkul, T.; Biswas, P. Role of surface area, primary particle size, and crystal phase on titanium dioxide nanoparticle dispersion properties. *Nanoscale Res. Lett.* **2010**, *6*, 1–8.

85. Gu, M.; Hao, L.; Wang, Y.; Li, X.; Chen, Y.; Li, W.; Jiang, L. The selective heavy metal ions adsorption of zinc oxide nanoparticles from dental wastewater. *Chem. Phys.* **2020**, *534*, 110750.

86. Yoshida, T. Leaching of zinc oxide in acidic solution. *Mater. Trans.* **2003**, *44*, 2489–2493.

87. Sheela, T.; Nayaka, Y.A.; Viswanatha, R.; Basavanna, S.; Venkatesha, T.G. Kinetics and thermodynamics studies on the adsorption of Zn(II), Cd(II) and Hg(II) from aqueous solution using zinc oxide nanoparticles. *Powder Technol.* **2012**, *217*, 163–170.

88. Rodríguez, C.; Tapia, C.; Leiva-Aravena, E.; Leiva, E. Graphene oxide–zno nanocomposites for removal of aluminum and copper ions from acid mine drainage wastewater. *Int. J. Environ. Res. Public Health* **2020**, *17*, 1–18.

89. Lee, S.; Zhang, Z.; Wang, X.; Pfefferle, L.D.; Haller, G.L. Characterization of multi-walled carbon nanotubes catalyst supports by point of zero charge. *Catal. Today* **2011**, *164*, 68–73.

90. Pyrzyńska, K.; Bystrzejewski, M. Comparative study of heavy metal ions sorption onto activated carbon, carbon nanotubes, and carbon-encapsulated magnetic nanoparticles. *Colloids Surf. A Physicochem. Eng. Asp.* **2010**, *362*, 102–109.

91. Hu, J.; Shipley, H.J. Evaluation of desorption of Pb (II), Cu (II) and Zn (II) from titanium dioxide nanoparticles. *Sci. Total Environ.* **2012**, *431*, 209–220.

92. Grover, V.A.; Hu, J.; Engates, K.E.; Shipley, H.J. Adsorption and desorption of bivalent metals to hematite nanoparticles. *Environ. Toxicol. Chem.* **2012**, *31*, 86–92.

93. Lim, J.L.; Okada, M. Regeneration of granular activated carbon using ultrasound. *Ultrason. Sonochem.* **2005**, *12*, 277–282.

94. Rege, S.U.; Yang, R.T.; Cain, C.A. Desorption by ultrasound: Phenol on activated carbon and polymeric resin. *AIChE J.* **1998**, *44*, 1519–1528.

95. Breitbach, M.; Bathen, D.; Schmidt-Traub, T. Effect of ultrasound on adsorption and desorption processes. *Ind. Eng. Chem. Res.* **2003**, *42*, 5635–5646.

96. Korkut, O.; Sayan, E.; Lacin, O.; Bayrak, B. Investigation of adsorption and ultrasound assisted desorption of lead (II) and copper (II) on local bentonite: A modelling study. *Desalination* **2010**, *259*, 243–248.

97. Yousefi, A.; Allahverdi, A.; Hejazi, P. Effective dispersion of nano-TiO2 powder for enhancement of photocatalytic properties in cement mixes. *Constr. Build. Mater.* **2013**, *41*, 224–230.

98. Ma, J.; Zuo-Jiang, S.; He, Y.; Sun, Q.; Wang, Y.; Liu, W.; Sun, S.; Chen, K. A facile, versatile approach to hydroxyl-anchored metal oxides with high Cr (VI) adsorption performance in water treatment. *R. Soc. Open Sci.* **2016**, *3*, 160524.

99. MiarAlipour, S.; Friedmann, D.; Scott, J.; Amal, R. TiO2/porous adsorbents: Recent advances and novel applications. *J. Hazard. Mater.* **2018**, *341*, 404–423.

100. Foo, K.Y.; Hameed, B.H. Insights into the modeling of adsorption isotherm systems. *Chem. Eng. J.* **2010**, *156*, 2–10.

101. Saadi, R.; Saadi, Z.; Fazaeli, R.; Fard, N.E. Monolayer and multilayer adsorption isotherm models for sorption from aqueous media. *Korean J. Chem. Eng.* **2015**, *32*, 787–799.

102. Amin, M.T.; Alazba, A.A.; Shafiq, M. Nonspontaneous and multilayer adsorption of malachite green dye by Acacia nilotica waste with dominance of physisorption. *Water Sci. Technol.* **2017**, *76*, 1805–1815.

103. Zhang, X.; Ge, Y.; Zhu, G.; Tang, J.; Xing, X.; Li, N. Effect of acid and hydrothermal treatments on the multilayer adsorption of Cr(VI) and dyes on biomass-derived nano/mesoporous carbon. *J. Mater. Res.* **2019**, *34*, 3020–3029.

104. Zeldowitsch, J. Adsorption site energy distribution. *Acta Phys. Chim. URSS* **1934**, *1*, 961–973.

105. Cuppett, J.D.; Duncan, S.E.; Dietrich, A.M. Evaluation of copper speciation and water quality factors that affect aqueous copper tasting response. *Chem. Senses* **2006**, *31*, 689–697.

106. Prolongo, S.G.; Rosario, G.; Urena, A. Study of the effect of substrate roughness on adhesive joints by SEM image analysis. *J. Adhes. Sci. Technol.* **2006**, *20*, 457–470.

107. Simonin, J.P. On the comparison of pseudo-first order and pseudo-second order rate laws in the modeling of adsorption kinetics. *Chem. Eng. J.* **2016**, *300*, 254–263.

108. Khezamia, L.; Tahaa, K.K.; Amamic, E.; Ghiloufid, I.; El Mird, L. Removal of cadmium (II) from aqueous solution by zinc oxide nanoparticles: Kinetic and thermodynamic studies. *Desalin. Water Treat.* **2017**, *62*, 346–354.

109. Zhang, F.; Lan, J.; Yang, Y.; Wei, T.; Tan, R.; Song, W. Adsorption behavior and mechanism of methyl blue on zinc oxide nano-particles. *J. Nanoparticle Res.* **2013**, *15*, 1–10.

110. Sigma-Aldrich. Zinc Oxide, Dispersion. Available online: https://www.sigmaaldrich.com/CL/es/product/aldrich/721077?context=product (accessed on 22 September 2021).

111. Sigma-Aldrich. Graphene Powder. Available online: https://www.sigmaaldrich.com/CL/es/product/aldrich/900561?context=product (accessed on 22 September 2021).

112. Sigma-Aldrich. Carbon Nanotube, Multi-Walled. Available online: https://www.sigmaaldrich.com/CL/es/product/aldrich/698849?context=product (accessed on 22 September 2021).